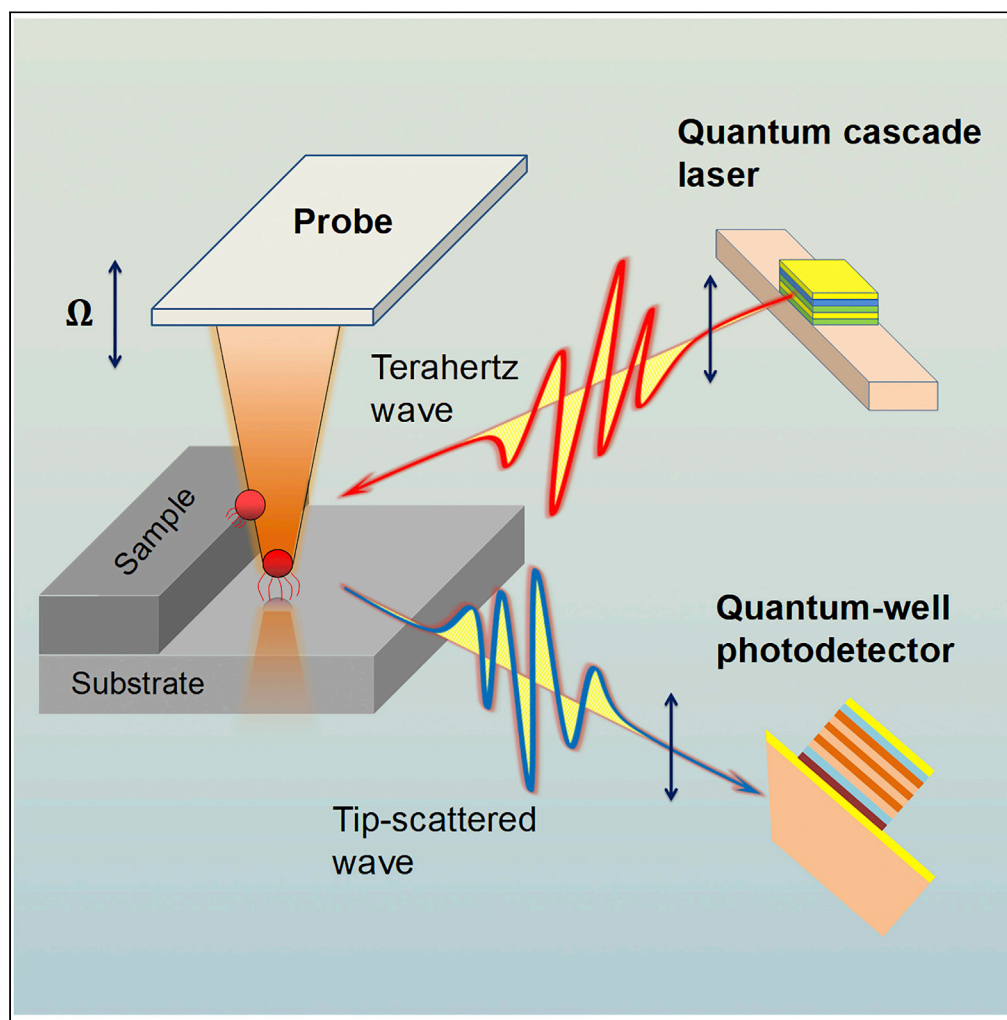


## Article

## A terahertz near-field nanoscopy revealing edge fringes with a fast and highly sensitive quantum-well photodetector



Fucheng Qiu,  
Guanjun You,  
Zhiyong Tan, ...,  
Zhanglong Fu,  
Hua Li, Juncheng  
Cao

zytan@mail.sim.ac.cn (Z.T.)  
cwang@mail.sim.ac.cn (C.W.)  
jccao@mail.sim.ac.cn (J.C.)

**Highlights**

THz scattering-type  
scanning near-field optical  
microscope with a high-  
power THz QCL

Highly sensitive THz  
quantum-well  
photodetector for  
effective signal collection

Nanoscale spatial  
resolution reveals local  
optical properties in THz  
range

Experimentally  
investigate and  
theoretically interpret the  
formation of the edge  
fringes

Qiu et al., iScience 25, 104637  
July 15, 2022 © 2022 The  
Authors.  
[https://doi.org/10.1016/  
j.isci.2022.104637](https://doi.org/10.1016/j.isci.2022.104637)

## Article

## A terahertz near-field nanoscopy revealing edge fringes with a fast and highly sensitive quantum-well photodetector

Fucheng Qiu,<sup>1,2,7</sup> Guanjun You,<sup>3,7</sup> Zhiyong Tan,<sup>1,\*</sup> Wenjian Wan,<sup>1</sup> Chang Wang,<sup>1,\*</sup> Xiao Liu,<sup>3</sup> Xinzhong Chen,<sup>4</sup> Rui Liu,<sup>5</sup> Hu Tao,<sup>6</sup> Zhanglong Fu,<sup>1</sup> Hua Li,<sup>1</sup> and Juncheng Cao<sup>1,8,\*</sup>

## SUMMARY

**We demonstrate the successful implementation of a terahertz (THz) quantum-well photodetector (QWP) for effective signal collection in a scattering-type scanning near-field optical microscope (s-SNOM) system. The light source is an electrically pumped THz quantum cascade laser (QCL) at 4.2 THz, which spectrally matches with the peak photoresponse of THz QWP. The sensitive THz QWP has a low noise equivalent power (NEP) of about 1.1 pW/Hz<sup>0.5</sup> and a spectral response range from 2 to 7 THz. The fast-responding capability of the THz QWP is vital for detecting the rapidly tip-modulated THz light which can effectively suppress the background noise. The THz images of the nanostructure demonstrate a spatial resolution of about 95 nm, corresponding to  $\sim\lambda/752$  at 4.2 THz. We experimentally investigate and theoretically interpret the formation of the fringes which appear at the edge position of a gold stripe in the THz near-field image.**

## INTRODUCTION

Terahertz (THz) imaging (Jelic et al., 2017; Nagatsuma, 2011) has attracted remarkable interest because of the distinct superiority in non-destructive examination (Haaser et al., 2013; Novikova et al., 2018; Ahi et al., 2017), biomedical sensing (Kim et al., 2006), and security checking (Ok et al., 2014). However, due to the diffraction limit, the spatial resolution of conventional THz imaging systems is restricted to the sub-millimeter scale, which is not capable of nano-optical imaging of the fine structures. In recent years, the scattering-type scanning near-field optical microscopy (s-SNOM) (Jiang et al., 2018b; Seebacher et al., 2001; Chen et al., 2019) has become an effective tool in the nanoscale research of the semiconductor (Schmidt et al., 2018; Madapu et al., 2018; Fei et al., 2012), plasmonic (Wagner et al., 2014; Lang et al., 2018), biology (Jiang et al., 2018a), and dielectric systems (Atkin et al., 2012). Usually, a sharp scanning probe of atomic force microscopy (AFM) (Klarskov et al., 2017) is placed in the vicinity of the sample surface to acquire high spatial frequency (momentum) properties. Nanoscale resolution can be obtained by using an s-SNOM operating at frequencies from visible to microwave (Liewald et al., 2018).

Current THz technology can be readily combined with s-SNOM to improve the resolution of the THz imaging system (Moon et al., 2015). In terms of imaging applications, the THz quantum-cascade laser (QCL) (Degl'Innocenti et al., 2017; Dean et al., 2016; Giordano et al., 2018) is of more interest due to its advantages in high output power, beam quality, and electrical pumping scheme, especially in the spectral range from 2 to 5 THz, well beyond the capability of common THz sources such as photoconductive antenna (Zhang et al., 2018) and Schottky diodes (Chen et al., 2020). However, highly sensitive THz detectors with large spectral response range and rapid detection capability are still in short supply.

The THz quantum-well photodetector (QWP) (Guo et al., 2013) can solve these problems due to its special advantages including the fast temporal response, high sensitivity, and mature fabrication technology. For n-type QWPs, the THz radiation can induce the intersubband transition (ISBT) of confined electrons in the multi quantum wells (MQWs). Owing to the intrinsic short lifetime of the photocarriers, the THz QWPs typically has a response time at the picosecond level. The polarization of THz QWP and THz QCL can be designed to be consistent with each other to improve the collection efficiency of the THz wave. Therefore, THz QCLs can be applied in the THz imaging (Qiu et al., 2019) in conjunction with the frequency-matched THz QWPs. Compared with the time-domain spectrometer (TDS)-based commercial s-SNOM setup (Neaspec

<sup>1</sup>Laboratory of Terahertz Solid-State Technology, Shanghai Institute of Microsystem and Information Technology, Chinese Academy of Sciences, Shanghai 200050, and Center of Materials Science and Optoelectronics Engineering, University of Chinese Academy of Sciences, Beijing 100049, China

<sup>2</sup>Chongqing Institute of Green and Intelligent Technology, Chinese Academy of Sciences, Chongqing 400714, and Chongqing School, University of Chinese Academy of Sciences, Chongqing 400714, China

<sup>3</sup>Shanghai Key Lab of Modern Optical Systems, Terahertz Technology Innovation Research Institute, and Engineering Research Center of Optical Instrument and System, Ministry of Education, University of Shanghai for Science and Technology, Shanghai 200093, China

<sup>4</sup>Department of Physics and Astronomy, Stony Brook University, Stony Brook, NY 11794, USA

<sup>5</sup>Ithatron Instruments, Jiaying 314006, China

<sup>6</sup>State Key Laboratory of Transducer Technology, Shanghai Institute of Microsystem and Information Technology, Chinese Academy of Sciences, Shanghai 200050, China

<sup>7</sup>These authors contributed equally

<sup>8</sup>Lead contact

\*Correspondence: zytan@mail.sim.ac.cn (Z.T.), cwang@mail.sim.ac.cn (C.W.), jccao@mail.sim.ac.cn (J.C.)  
<https://doi.org/10.1016/j.isci.2022.104637>



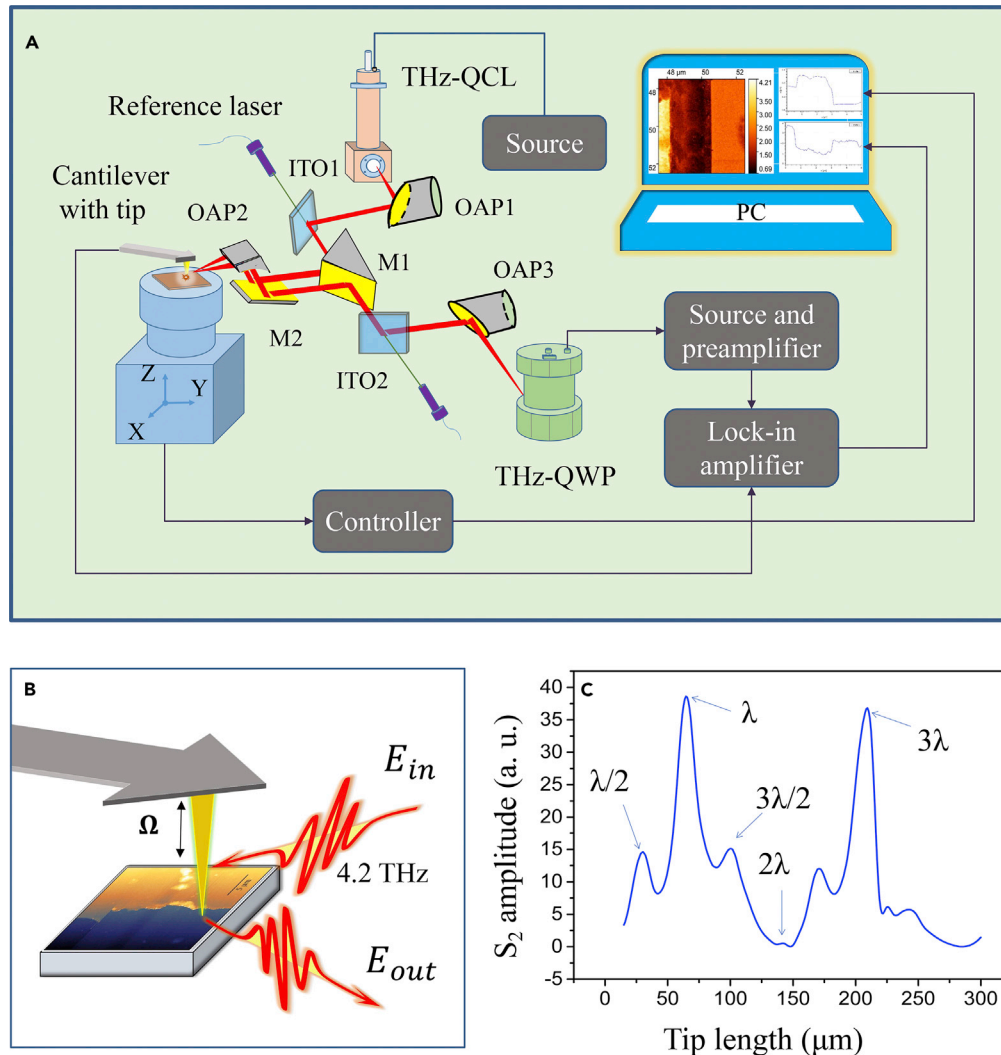


**Figure 1. The schematic of the THz s-SNOM setup and the numerical simulation of the THz electric-field intensity**  
(A) The THz near-field imaging system based on a high-power THz QCL and a fast THz QWP.  
(B) The conceptual representation of THz tip-scattered near-field imaging.  
(C) The simulated amplitude of the  $S_2$  signal with different tip lengths.

GmbH), the high-power QCL-based system is beneficial for the nanoscale observation of graphene plasmonics, polariton mapping in 2D materials, and subsurface chemical nano-identification. The combination of wide-spectrum THz QWPs with beam-combined monolithic THz QCL arrays (Chen et al., 2021) or QCL frequency comb technology (Li et al., 2020) potentially improves the spectral range and spectral resolution of the QCL-based s-SNOM. In this paper, we report a THz s-SNOM using a THz QCL emitting at 4.2 THz with an output power of over 3 mW and a fast and sensitive THz QWP employed as the detector. The spectral peak position in the photoresponse of the THz QWP can be accurately designed with the many-body effects. A spatial resolution of about 95 nm is experimentally demonstrated to be feasible.

## RESULTS

### Experimental setup of THz s-SNOM

The schematic of the THz s-SNOM setup is shown in Figure 1A. This THz near-field imaging system operates in the self-homodyne scheme (Wehmeier et al., 2020; de Oliveira et al., 2020) with a bilateral symmetric light path and no asymmetric Michelson interferometer is used in order to minimize the loss of the THz energy as the beam splitter will cause at least three-quarters of the energy loss. The electrically pumped THz

QCL is placed in a cryostat at the temperature of 10 K and emits a 4.2 THz (red) beam. The humidity during the experiment is about 60%. With a visible laser (the green line shown in Figure 1A) employed as a guide of the THz beam, the divergent THz beam is collimated by an off-axis parabolic mirror (OAP1), then reflected by an indium tin oxide (ITO) glass and two planar reflecting mirrors (M1 and M2), and finally focused by an off-axis parabolic mirror (OAP2) onto the apex of a metallic tip. The scattered THz beam is collected by OAP2 and then reflected by M2, M1, and ITO2, before it is focused onto the THz QWP by another off-axis parabolic mirror (OAP3). The off-axis parabolic mirrors in the experiment own a same focal length of about 50 mm. The expected waist radius of the focused spot is 200  $\mu\text{m}$ . The reflectance of ITO mirrors at 4.2 THz is estimated to be about 85% by measured the power ratio before and after reflection.

When the THz beam illuminates the object from the far-field, a propagating field and a non-radiating field can be induced from the object. Although the propagating field can be detected by a far-field detector, the non-radiating field with high spatial frequency information of the object is confined within the near-field space and will decrease exponentially as the distance increases. The apex of the probe in the vicinity of the surface can generate an enhancement of the optical near-field intensity. To qualitatively understand the signal contrast mechanism, we resort to the simplest model where the tip is approximated as a polarizable sphere (Knoll and Keilmann, 1999). The electric field of the scattered near-field signal  $E_s$  can be expressed as

$$E_s = \alpha^{\text{eff}}(1 + \gamma)^2 E_i \quad (\text{Equation 1})$$

where  $\gamma$  is the far-field reflection coefficient of the sample surface, and can be well-approximated by the Fresnel reflection under the circumstances of p-polarized light (Dai et al., 2018). The effective polarizability  $\alpha^{\text{eff}}$  of the tip-sample junction can be given by

$$\alpha^{\text{eff}} = \frac{\alpha(1 + \beta)}{1 - \frac{\alpha\beta}{16\pi(a + d)^3}} \quad (\text{Equation 2})$$

where  $a$  is the radius of the tip and  $d$  is the distance between the tip and the sample. The bare polarizability of the tip  $\alpha$  and the dielectric response function of the sample  $\beta$  are given by

$$\alpha = 4\pi a^3 \frac{\epsilon_t - 1}{\epsilon_t + 2} \quad (\text{Equation 3})$$

$$\beta = \frac{\epsilon_s - 1}{\epsilon_s + 1} \quad (\text{Equation 4})$$

where  $\epsilon_t$  and  $\epsilon_s$  represent the dielectric constants of the tip and the sample, respectively.

It is important for the terahertz near-field imaging system to acquire the high spatial frequency information from the objects. The THz light, emitted by the THz QCL with a waist radius of about 300  $\mu\text{m}$ , is focused onto the sample and the tip of an AFM probe which operates in tapping mode. The scattered THz beam is modulated by dithering the probe near its mechanical resonant frequency  $\Omega$ . The modulated probe can enhance the near-field signal and transform the near-field signal to the far-field  $E_r + E_s(\Omega)$ , as sketched in Figure 1B. A high-order demodulation method is applied in the experiment to demodulate the scattered signal at higher harmonics of  $\Omega$  in order to effectively suppress the background noise. The THz QWP is employed to detect the tip-scattered near-field THz signal in the far-field region. The detected signal of the THz QWP is amplified by a preamplifier and subsequently demodulated by a lock-in amplifier at the  $n$ th harmonics of the tip-tapping frequency  $\Omega$ , which results in different orders of the tip-scattered near-field signal  $S_n$ .

In order to demonstrate the tip enhancement effect at the frequency of 4.2 THz, a method of moment solver (MoM) (Altair Feko) is employed to simulate the change of  $S_2$  signal with different tip length (see the Method details section). As shown in Figure 1C, multiple resonances analogous to dipole antenna resonances corresponding to integer multiples of the half-wavelength can be observed, consistent with previous study (Mastel et al., 2017). In our experiment, a platinum tip (Rocky Mountain Nanotechnology, LLC) of shank length about 80  $\mu\text{m}$  and mechanical resonance frequency  $\Omega$  about 13 kHz is used in the system to enhance the THz scattering and improve the signal-to-noise ratio. The tapping amplitude of the tip is about 300 nm.

### Device performance of THz-QWP

The schematic of the electrically pumped THz QCL and the typical 45° facet light-coupling THz QWP are shown in Figure 2A. The THz light emitted by the THz QCL can be well coupled into the MQW region with

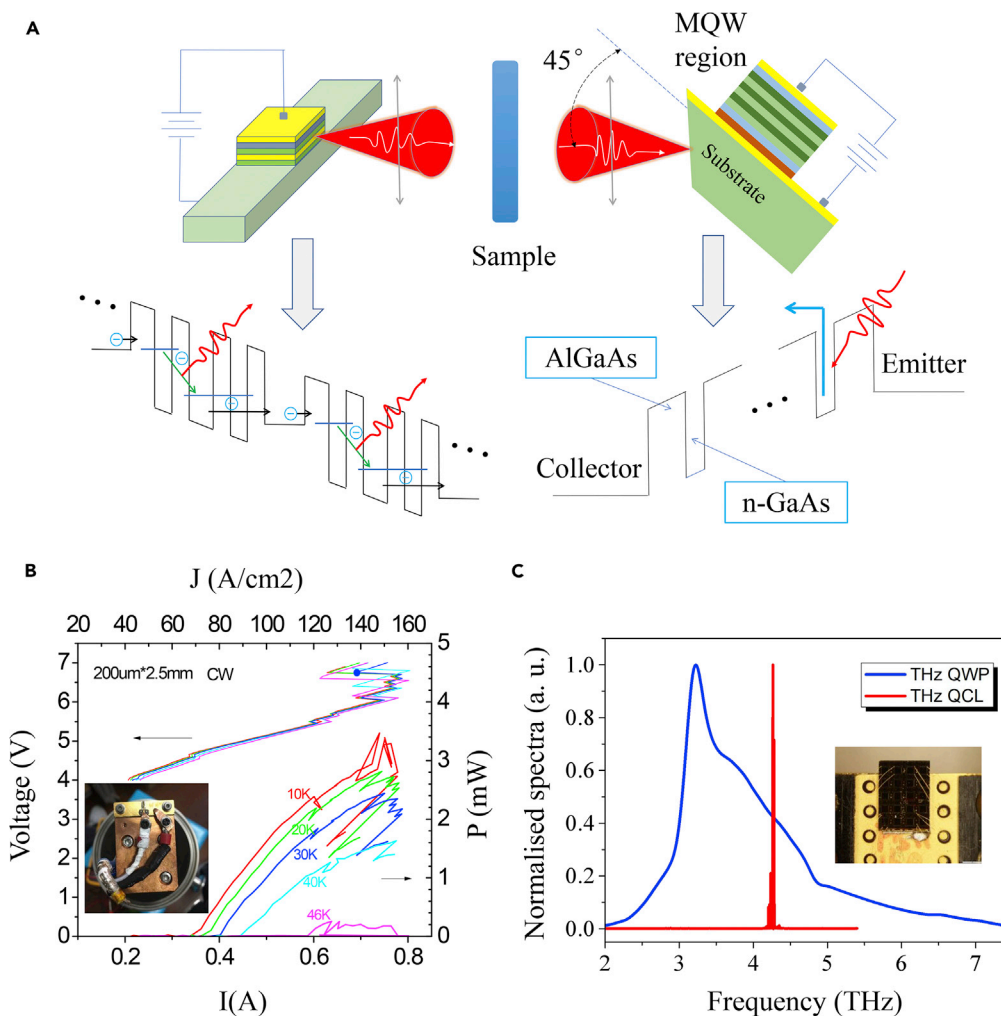


**Figure 2. The schematic diagram and device performance of the THz QCL and the THz-QWP**

(A) The schematics and typical band structures for both the continuous electrically pumped THz QCL and the 45° facet light-coupled THz QWP.

(B) The output power and the current density of the THz QCL at different temperatures. Inset: one photograph of the THz QCL chip.

(C) The emission spectra of the 4.2 THz QCL and the photocurrent spectra of the frequency-matched THz QWP. Inset: one photograph of the THz QWP chip.

a 45° edge facet geometry. The sensitive area of the QWP detector is  $400 \times 400 \mu\text{m}$ . The THz detection is achieved by measuring the photocurrent of THz QWP that excited by the THz radiation. It is worth noting that the vertical polarization (p-polarization) of the incident light can improve the tip enhancement effect (Jelic et al., 2017). So, the vertically polarized THz QCL and THz QWP are employed in the THz s-SNOM system to maximize the THz near-field signal. The common band structure of the THz QCL and THz QWP is exhibited at the bottom of the Figure 2A. The sample growth and device fabrication methods of the THz QCL and THz QWP are described in the method details section. The THz QCL can generate 3 mW power when operating in continuous wave mode at a drive current (density) of 770 mA ( $150 \text{ A/cm}^2$ ), as shown in Figure 2B. The results demonstrate that the THz output power decreases as the temperature increases. 10 K is employed in the experiment to ensure the maximum power for optimal signal-to-noise ratio. The inset of the Figure 2B exhibits the photograph of the THz QCL device which is mounted on the cold head of the cryostat.

In order to match the photoresponse with the QCL emission, the many-body effects including the interactions among electrons and those between electrons and other quasiparticles are fully considered when

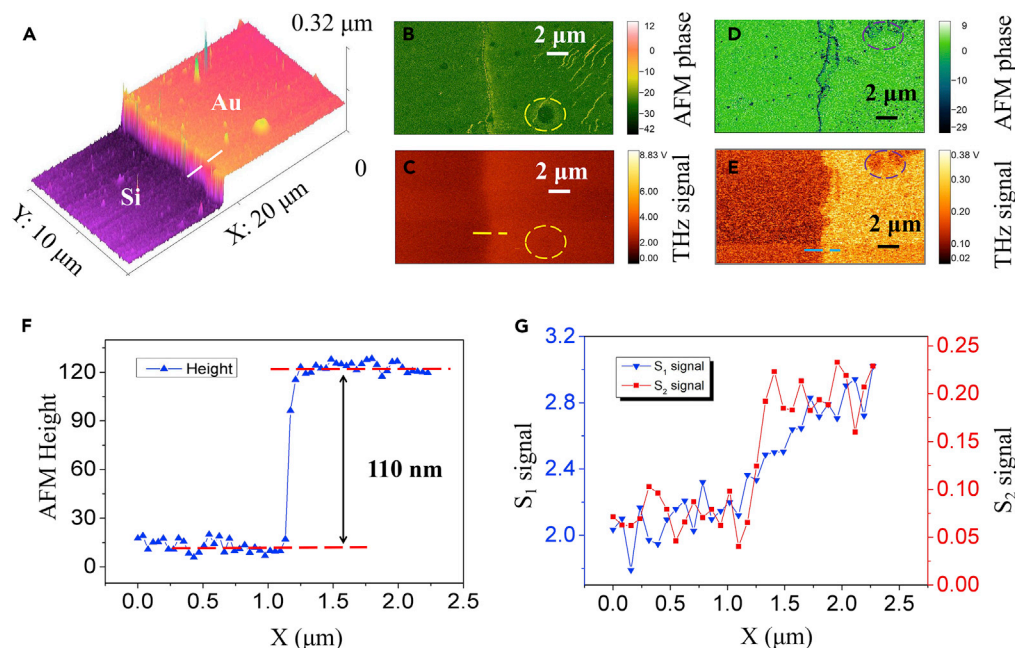


**Figure 3. Nano-imaging of the gold film interface on a Si substrate**

(A–C) The AFM topography, AFM phase, and THz near-field images of the interface with the  $S_1$  THz signal.

(D and E) The AFM phase and THz near-field images of another part of the interface with the  $S_2$  THz signal.

(F) The height value along the yellow line in Figure 3A. (G) The THz signal amplitude along the yellow line in Figure 3C and the blue line in Figure 3E.

designing and optimizing the MQW structure (Guo et al., 2009; Wang et al., 2018). By self-consistently solving the coupled Schrödinger and Poisson equations, the absorption efficiency  $\eta$  can be derived as

$$\eta(\omega) = \frac{\pi e^2}{\epsilon_0 c n_0 \omega m^{*2}} \sum_j \int \frac{dK}{(2\pi)^3} | \langle j | p_z | 0 \rangle |^2 [f(E_{k,0}, \epsilon_f, T) - f(E_{k,j}, \epsilon_f, T)] \delta(\Delta \tilde{E}_{k,l,0} - \hbar\omega) \quad (\text{Equation 5})$$

where  $\epsilon_0$  is the vacuum permittivity,  $c$  is the speed of the light,  $n_0$  is the refractive index,  $m^*$  is the electron effective mass,  $p_z$  is momentum,  $f$  is the Fermi distribution function,  $E_{k,l}$  is the energy of the electron at different subband index  $l$ ,  $\epsilon_f$  is the Fermi energy,  $T$  is temperature, and  $\Delta \tilde{E}_{k,l,0}$  is the energy difference between the  $j$ th and the ground subbands. The emission spectra of the 4.2 THz QCL and the photocurrent spectra of the frequency-matched THz QWP are both presented in Figure 2C which are characterized by a Fourier transform infrared spectrometer (FTIR). The results show that the THz QCL can match the THz QWP response at the frequency of 4.2 THz. The photograph of the THz QWP chip is shown in the inset of Figure 2C.

The temporal response of the THz QWP is on the level of picosecond due to the short lifetime of photo-excited electrons (Guo et al., 2013), which is very important in the effective detection of the high-speed-modulated THz signals. The high-frequency performances of the THz QWP are studied by employing a microwave rectification technique (Li et al., 2017). The THz QWP can detect up to 6.2 GHz-modulated THz light generated by the THz QCL, which is sufficient for detecting the tip-modulated scattered light. On the other hand, the detector of the THz s-SNOM must possess enough sensitivity to respond properly to the scattered near-field signal which is about one-thousandth in power of the far-field signal. The noise equivalent power (NEP) parameter of the THz QWP is calculated based on the values of the noise spectral density and peak responsivity (see the Method details section). A NEP of about  $1.1 \text{ pW/Hz}^{0.5}$  can be estimated at the bias voltage of 40 mV. The device performances of the THz QCL and the THz QWP exhibit the applicability to the fast THz imaging system (Qiu et al., 2019).

## DISCUSSION

As a demonstration of the s-SNOM performance, we first perform the nano-imaging of a gold film deposited on a silicon substrate which owns a resistivity of about  $1 \times 10^4 \Omega \cdot \text{cm}$ . The AFM topography, AFM phase, and THz near-field  $S_1$  images of the interface are shown in Figures 3A–3C, respectively. One can observe

that a defect in the Au area is legible in [Figures 3A and 3B](#), but not in [Figure 3C](#). When the  $S_2$  signal is utilized to characterize another part of the interfaces, an obvious imperfection is clearly seen in the AFM phase and THz near-field  $S_2$  images, as shown in [Figures 3D and 3E](#). The results indicate that the higher order demodulation of the THz signal is needed to sufficiently suppress the undesired far-field background signal. [Figure 3F](#) exhibits the height value along the white line in [Figure 3A](#), from which one can obtain a height difference of about 110 nm in the boundary between the Si and Au. [Figure 3G](#) gives the THz signal amplitude along the yellow line in [Figure 3C](#) and the blue line in [Figure 3E](#). A relative THz signal value of 0.75 and 0.15 V can be estimated from the  $S_1$  and  $S_2$  signals, respectively. A sharper rise can be observed in the change of  $S_2$  signal which is 5–10 times weaker than the  $S_1$  signal.

The signal-to-noise ratio (SNR) of the  $S_1$  and  $S_2$  signal is evaluated to be 8 and 4 by dividing the averaging signal from panels by the noise from pane ([Figure 3G](#)). The SNR of  $S_3$  is evaluated to be about 1 from the image of the gold film region, as exhibited in [Figure S1](#). In order to acquire higher spatial resolution, a probe with a radius of about 20 nm was employed which reduced the SNR to some extent. The SNR of  $S_2$  signal is similar to that in the near-field systems reported in references ([Degl'Innocenti et al., 2017](#); [Dean et al., 2016](#); [Giordano et al., 2018](#)) at the same resolution level (<100 nm). The optical properties of the sample can usually be extracted from the contrast between the sample and material with known dielectric permittivity ([Moon et al., 2011](#); [Guo et al., 2021](#); [McLeod et al., 2014](#)). The contrast of  $S_2$  signal between the Au and Si substrate is evaluated to be about 3.5 which is similar to the  $S_2$  contrast ( $\sim 3$ ) and lower than the  $S_3$  contrast ( $\sim 4$ ) in previous report ([Pogna et al., 2021](#)) due to the influence of the background signal.

To quantitatively determine the spatial resolution of the THz near-field imaging system, a sample of gold nanostructures with a width of  $\sim 1.5 \mu\text{m}$  is imaged, and the results are presented in [Figure 4](#). The AFM topography, AFM phase, and THz near-field images of the gold bars on Si substrate are presented in [Figures 4A–4C](#), respectively. A height difference of about 110 nm can be calculated from the signal change over the white line in [Figure 4A](#), as exhibited in [Figure 4D](#). The amplitude of the THz near-field signal ( $S_2$ ) along the black line in the THz image is plotted in [Figure 4E](#). A spatial resolution of about 95 nm, corresponding to  $\sim \lambda/752$  at 4.2 THz, is achieved based on the full-width-at-half-maximum of the derivative function of the fitting result (red curve in the inset of [Figure 4E](#)). Finer sampling can be employed when higher resolution levels are achieved. The measurement may contain imaging artifacts due to the step in topography, potentially resulting in an overmeasure or underestimation. A sample with sharp material boundary and ultrasmooth surface can help reduce the influence of the artifacts ([Mastel et al., 2018](#); [Mooshammer et al., 2020](#)). A simulation using MoM of a tip raster scanning over the Si-Au interface is performed. A spatial resolution on the level of the experimental result can be obtained from the Gaussian curve interpolating the derivative function, as shown in [Figure 4F](#). The available resolution almost depends on the radius of the tip and the sensitivity of the detector. Higher resolution can be obtained by employing a smaller tip at the same harmonic. On the other hand, purer near-field signal can be collected with higher harmonics, which results in better resolution and requires more sensitive detectors at the same time.

The capability of scanning an uneven sample is an important attribute to evaluate the system performance of the s-SNOM. The images, with a size of  $50 \mu\text{m}$  by  $30 \mu\text{m}$  ( $256 \times 154$  pixels), of a gold sample is acquired by the THz near-field imaging system, as exhibited in [Figure S2](#). The scanning rate of AFM, including the process of going forth and back, is set to be 0.05 Hz/line. The scanning time of a pixel can be calculated to be about 39 ms which represents signal acquisition and integration. The longer pixel time is almost due to the time-consuming signal acquisition process of the preamplifier. A scratch, with a width of  $15 \mu\text{m}$ , can be easily distinguished in both the AFM topography and THz near-field images, as shown in [Figures S2A and S2B](#). Interestingly, the fine structure of the scratch can be observed in the THz near-field image but is not visible in the AFM topography image. [Figure S2C](#) gives the height value along the red line in [Figure S2A](#) and THz signal amplitude along the blue line in [Figure S2B](#). An obvious signal variation and good position consistent can be observed both in the height value and the THz signals, especially in the edge of the scratch. And the THz signals can provide more variation than the height value inside the scratch.

In order to particularly demonstrate the near-field variation in the edges of materials, an optical grating object with a gold plateau edge on a silicon substrate is imaged using the THz nanoscopy, with the results shown in [Figure 5](#). The AFM topography and THz near-field image of the grating edge are exhibited in

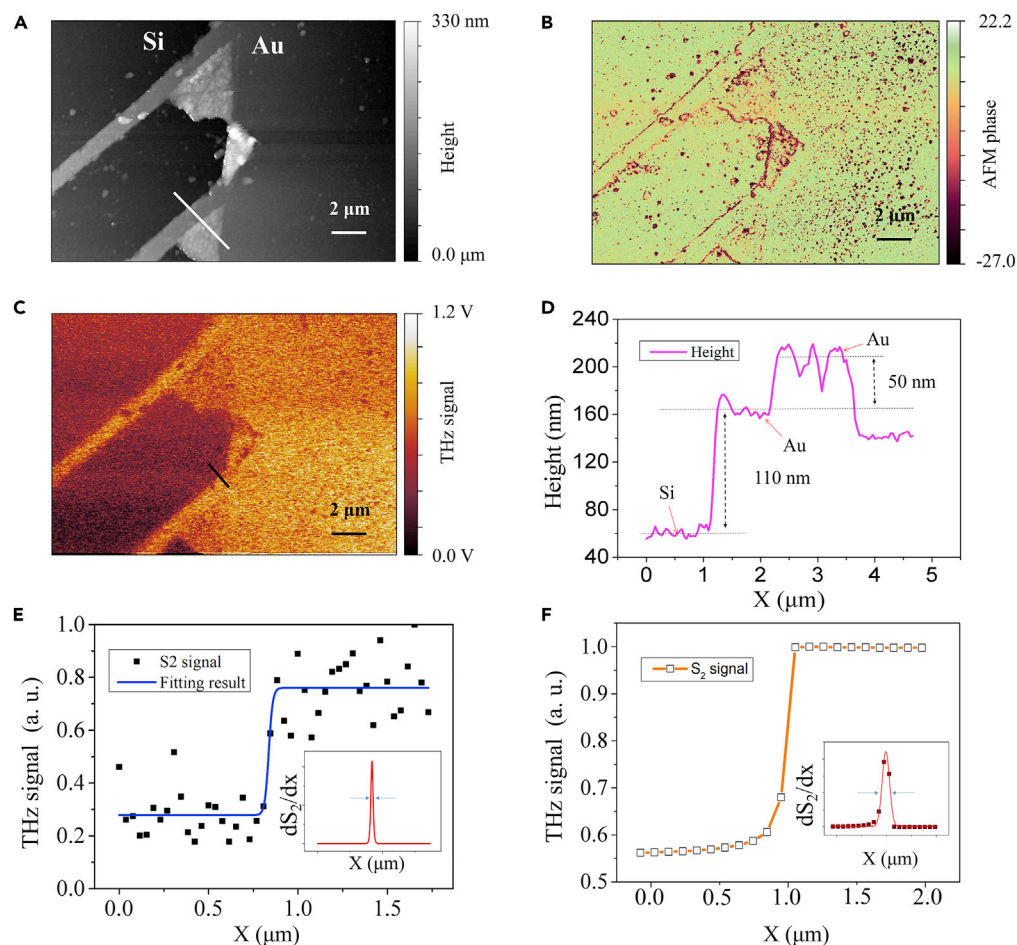


**Figure 4. Nano-imaging of the Au bars on a Si substrate**

(A–C) The AFM topography, AFM phase, and THz near-field images of the gold structure.

(D) The change of the height value over the white line in the AFM topography image.

(E) The amplitude and fitted results of the THz near-field signal ( $S_2$ ) along the black line in the THz image. Inset: derivative function of the fitting result.

(F) The simulation result of a tip scans over a gold-Si interface. Inset: derivative function of the  $S_2$  signal and fitted results.

Figures 5A and 5B, respectively. The SNR of the  $S_2$  signal is estimated to be about 10 with a thicker probe ( $\sim 80$  nm). Some edge fringes can be clearly observed in the THz image, especially at the interface of the grating. We pay special attention to the outside dark fringes and the bright fringes in the plateau of the edge. These fringes are different from those in the visible range, where gold supports plasmonic modes. Gold fringes in the THz range are not affected by the edge resonances.

The numerical simulation results of the edge fringes, as depicted in Figures 5D–5G, show that THz light is highly concentrated locally at the gap between the tip apex and the sample. The electric field strength between the tip and gold (Figure 5D) is stronger than that between the tip and the silicon substrate (Figure 5G). When the tip scans the edge of the grating (Figure 5E), two hot spots are formed: one right under the tip and one at the upper sharp edge of the sample (Abate et al., 2016). Because of these two hot spots, the THz near-field scattered signals can be increased and a bright fringe appears in the edge region (Figure 5C). An extensive scanning of a gentle edge is provided in Figure S3 which only shows the outside dark fringes. When the probe tip moves away from the plateau (Figure 5F), the apex does not couple to the silicon substrate right beneath it due to the curved profile (Babicheva et al., 2016). The smaller refractive index environment reduces the effective polarizability of the tip and forms an outside dark fringe in the near-field image of the edge. To explain the absence of the dark fringes in Figure 3, we compare the topography and the SNR of the step. The using of smaller tip, steeper interface, and larger

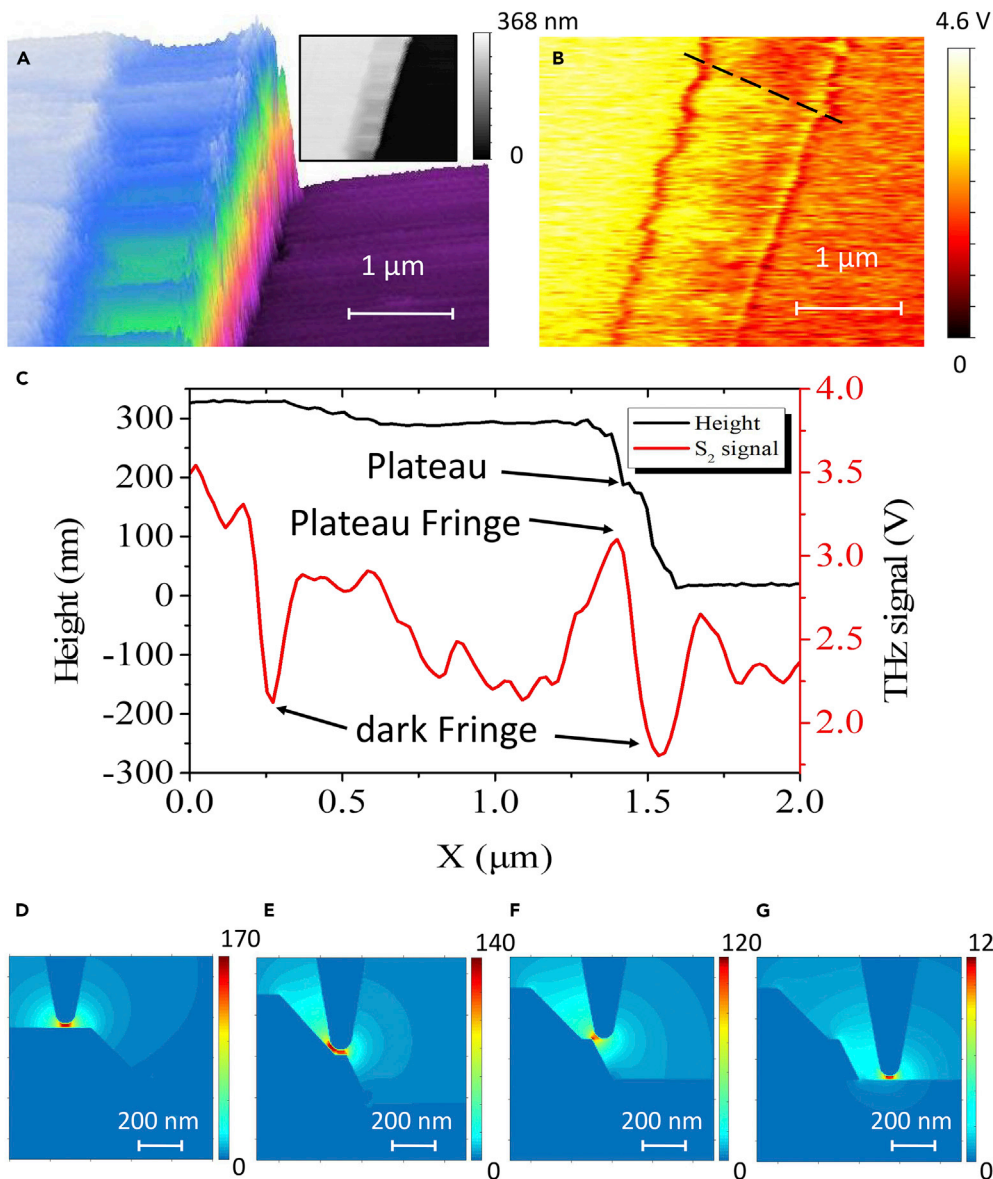


**Figure 5. Edge fringe nanoscopy**

(A and B) The AFM topography and THz near-field image of an optical grating object.  
(C) Line profiles taken from AFM topography and THz image for gold grating on silicon.  
(D–G) Theoretical simulation of the edge fringe formation.

scanning step in Figure 3 potentially reduces the possibility of scanning the sharp step and the intensity of the signal change. On the other hand, the signal changes obscured by the noise will become more pronounced due to the increase of SNR.

In summary, we report the implementation of a THz s-SNOM based on a fast responding and sensitive THz QWP. The THz QWP, with an accurate spectral design, can well match spectrally a high-power THz QCL at 4.2 THz. This pair of quantum devices is demonstrated to be a solid solution for THz near-field imaging system in the frequency range above 3 THz. The natural polarization characteristics of the THz QCL and THz QWP are beneficial to improve the tip-coupling efficiency of the THz near-field signal. A resolution of about 95 nm is obtained by imaging a sample of gold nanostructures. We further investigate the edge fringes formation in the THz images of a grating object. THz QWPs with higher coupling efficiency can be designed

and employed to improve the SNR of the THz s-SNOM system. We envision in the future the THz s-SNOM will become a powerful tool for the near-field imaging of the nanomaterials and biomedical samples in the frequency range from 2 to 5 THz.

### Limitations of the study

The measurement of spatial resolution may contain the influence of imaging artifacts which can be reduced by using a sample with sharp material boundary and ultrasmooth surface. The spatial resolution and imaging contrast are limited by the SNR of higher order signal and can be further improved by employing higher power THz sources, more sensitive detectors, and more efficient probes. Working in dry air or nitrogen environment may help reduce the influence of water vapor. Owing to the self-homodyne scheme, the system cannot accurately recognize the phase information of the sample. Other interferometric detection scheme such as homodyne and pseudo-heterodyne can be implemented to enable the phase-resolved capability, identify signal spatial fringes, and enhance the imaging contrast.

### STAR★METHODS

Detailed methods are provided in the online version of this paper and include the following:

- KEY RESOURCES TABLE
- RESOURCE AVAILABILITY
  - Lead contact
  - Material availability
  - Data and code availability
- METHOD DETAILS
  - Sample growth and device fabrication
  - Performance characterizations of the devices
  - Simulation of the THz near-field signal
  - Data analyses

### SUPPLEMENTAL INFORMATION

Supplemental information can be found online at <https://doi.org/10.1016/j.isci.2022.104637>.

### ACKNOWLEDGMENTS

This research was supported by National Natural Science Foundation of China (61927813, 61975225, 62035014, 62004209); National Key R&D Program of China (2017YFF0106302); National Science Fund for Excellent Young Scholars (62022084); "From 0 to 1" Innovation Program of Chinese Academy of Sciences (ZDBS-LY-JSC009); Chongqing Science and Technology Commission (E1396103, E2316104); and Science and Technology Commission of Shanghai Municipality (21DZ1101102).

### AUTHOR CONTRIBUTIONS

F.C.Q. designed the study. G.J.Y. put forward the higher order demodulation method and the coupling mode of the imaging system. F.C.Q., X.L., R.L., and Z.Y.T. performed the construction of the imaging system and analyzed the experimental results. F.C.Q. and X.Z.C. designed the simulation and discussed the results. Z.L.F. and Z.Y.T. designed the QWP device and performed the characterizations. W.J.W., H.L., and C.W. designed the QCL device and performed the electrical and optical measurements. F.C.Q. wrote the manuscript with contributions from all other authors. G.J.Y., C.W., Z.Y.T., X.Z.C., H.T., H.L., and J.C.C. performed the revise of the manuscript. C.W., Z.Y.T., and J.C.C. supervised the project.

### DECLARATION OF INTERESTS

The authors declare no competing interests.

Received: November 21, 2021

Revised: May 15, 2022

Accepted: June 14, 2022

Published: July 15, 2022

## REFERENCES

- Abate, Y., Gamage, S., Li, Z., Babicheva, V., Javani, M.H., Wang, H., Cronin, S.B., and Stockman, M.I. (2016). Nanoscopy reveals surface-metallic black phosphorus. *Light Sci. Appl.* 5, 2095–5545. <https://doi.org/10.1038/lsa.2016.162>.
- Ahi, K., Shahbazmohamadi, S., and Asadizanjani, N. (2017). Quality control and authentication of packaged integrated circuits using enhanced-spatial-resolution terahertz time-domain spectroscopy and imaging. *Opt. Laser Eng.* 104, 274–284. <https://doi.org/10.1016/j.optlaseng.2017.07.007>.
- Atkin, J.M., Berweger, S., Jones, A.C., and Raschke, M.B. (2012). Nano-optical imaging and spectroscopy of order, phases, and domains in complex solids. *Adv. Phys.* 61, 745–842. <https://doi.org/10.1080/00018732.2012.737982>.
- Babicheva, V.E., Gamage, S., Stockman, M.I., and Abate, Y. (2016). Near-field edge fringes at sharp material boundaries. *Opt Express* 25, 23935–23944. <https://doi.org/10.1364/OE.25.023935>.
- Chen, X.Z., Hu, D.B., Mescall, R., You, G.J., Basov, D.N., Dai, Q., and Liu, M.K. (2019). Modern scattering-type scanning near-field optical microscopy for advanced material research. *Adv. Mater.* 31, 1804774. <https://doi.org/10.1002/adma.201804774>.
- Chen, X.Z., Liu, X., Guo, X.D., Chen, S., Hu, H., Nikulina, E., Ye, X.L., Yao, Z.H., Bechtel, H.A., Martin, M.C., et al. (2020). THz near-field imaging of extreme subwavelength metal structures. *ACS Photonics* 7, 687. <https://doi.org/10.1021/acsp Photonics.9b01534>.
- Chen, J., Jin, Y., Gao, L., Reno, J.L., and Kumar, S. (2021). Wavelength beam-combining of terahertz quantum-cascade laser arrays. *Opt. Lett.* 46, 1864–1867. <https://doi.org/10.1364/OL.420398>.
- Dai, G.B., Yang, Z.B., Geng, G.S., Li, M.L., Chang, T.Y., Wei, D.S., Du, C.L., Cui, H.L., and Wang, H.B. (2018). Signal detection techniques for scattering-type scanning near-field optical microscopy. *Spectrosc. Rev.* 53, 806–835. <https://doi.org/10.1080/05704928.2018.1443275>.
- de Oliveira, T.V.A.G., Nörenberg, T., Álvarez-Pérez, G., Wehmeier, L., Taboada-Gutiérrez, J., Obst, M., Hempel, F., Lee, E.J.H., Klopff, J.M., Errea, I., et al. (2020). Nanoscale-confined terahertz polaritons in a van der waals crystal. *Adv. Mater.* 33, 2005777. <https://doi.org/10.1002/adma.202005777>.
- Dean, P., Mitrofanov, O., Keeley, J., Kundu, I., Li, L., Linfield, E.H., and Davies, A.G. (2016). Apertureless near-field terahertz imaging using the self-mixing effect in a quantum cascade laser. *Appl. Phys. Lett.* 108, 091113. <https://doi.org/10.1063/1.4943088>.
- Degl'Innocenti, R., Wallis, R., Wei, B., Xiao, L., Kindness, S.J., Mitrofanov, O., Braeuninger-Weimer, P., Hofmann, S., Beere, H.E., and Ritchie, D.A. (2017). Terahertz nanoscopy of plasmonic resonances with a quantum cascade laser. *ACS Photonics* 4, 2150–2157. <https://doi.org/10.1021/acsp Photonics.7b00687>.
- Fei, Z., Rodin, A.S., Andreev, G.O., Bao, W., McLeod, A.S., Wagner, M., Zhang, L.M., Zhao, Z., Thieme, M., Dominguez, G., et al. (2012). Gate-tuning of graphene plasmons revealed by infrared nano-imaging. *Nature* 487, 82–85. <https://doi.org/10.1038/nature11253>.
- Giordano, M.C., Mastel, S., Liewald, C., Columbo, L.L., Brambilla, M., Viti, L., Politano, A., Zhang, K., Li, L., Davies, A.G., et al. (2018). Phase-resolved terahertz self-detection near-field microscopy. *Opt. Express* 26, 18423. <https://doi.org/10.1364/OE.26.018423>.
- Guo, X.G., Tan, Z.Y., Cao, J.C., and Liu, H.C. (2009). Many-body effects on terahertz quantum well detectors. *Appl. Phys. Lett.* 94, 201101. <https://doi.org/10.1063/1.3134485>.
- Guo, X.G., Cao, J.C., Zhang, R., Tan, Z.Y., and Liu, H.C. (2013). Recent progress in terahertz quantum-well photodetectors. *IEEE J. Sel. Top. Quantum Electron.* 19, 8500508. <https://doi.org/10.1109/JSTQE.2012.2201136>.
- Guo, X., Bertling, K., and Rakić, A.D. (2021). Optical constants from scattering-type scanning near-field optical microscope. *Appl. Phys. Lett.* 118, 041103. <https://doi.org/10.1063/5.0036872>.
- Haaser, M., Karrout, Y., Velghe, C., Cuppok, Y., Gordon, K.C., Pepper, M., Siepmann, J., Rades, T., Taday, P.F., and Strachan, C.J. (2013). Application of terahertz pulsed imaging to analyse film coating characteristics of sustained-release coated pellets. *Int. J. Pharm.* 457, 521–526. <https://doi.org/10.1016/j.ijpharm.2013.05.039>.
- Jelic, V., Iwaszczuk, K., Nguyen, P.H., Rathje, C., Hornig, G.J., Sharum, H.M., Hoffman, J.R., Freeman, M.R., and Hegmann, F.A. (2017). Ultrafast terahertz control of extreme tunnel currents through single atoms on a silicon surface. *Nat. Phys.* 13, 591–598. <https://doi.org/10.1038/nphys4047>.
- Jiang, X.J., Cai, W., Luo, W.W., Xiang, Y.X., Zhang, N., Ren, M.X., Zhang, X.Z., and Xu, J.J. (2018a). Near-field imaging of graphene triangles patterned by helium ion lithography. *Nanotechnology* 29, 385205. <https://doi.org/10.1088/1361-6528/aad0b4>.
- Jiang, J., Zhang, S., Qian, Z., Qin, N., Song, W., Sun, L., Zhou, Z., Shi, Z., Chen, L., Li, X., et al. (2018b). Protein bricks: 2D and 3D bio-nanostructures with shape and function on demand. *Adv. Mater.* 30, 1705919. <https://doi.org/10.1002/adma.201705919>.
- Kim, S.M., Hatami, F., Harris, J.S., Kurian, A.W., Ford, J., King, D., Scaleri, G., Giovannini, M., Hoyer, N., Faist, J., and Harris, G. (2006). Biomedical terahertz imaging with a quantum cascade laser. *Appl. Phys. Lett.* 88, 153903. <https://doi.org/10.1063/1.2194229>.
- Klarskov, P., Kim, H., Colvin, V.L., and Mittleman, D.M. (2017). Nanoscale laser terahertz emission microscopy. *ACS Photonics* 4, 2676. <https://doi.org/10.1021/acsp Photonics.7b00870>.
- Knoll, B., and Keilmann, F. (1999). Near-field probing of vibrational absorption for chemical microscopy. *Nature* 399, 134. <https://doi.org/10.1038/20154>.
- Lang, D., Balaghi, L., Winnerl, S., Schneider, H., Hübner, R., Kehr, S.C., Eng, L.M., Helm, M., Dimakis, E., and Pashkin, A. (2018). Nonlinear plasmonic response of doped nanowires observed by infrared nanospectroscopy. *Nanotechnology* 30, 084003. <https://doi.org/10.1088/1361-6528/aaf5a7>.
- Li, H., Wan, W.J., Tan, Z.Y., Fu, Z.L., Wang, H.X., Zhou, T., Li, Z.P., Wang, C., Guo, X.G., and Cao, J.C. (2017). 6.2-GHz modulated terahertz light detection using fast terahertz quantum well photodetectors. *Sci. Rep.* 7, 3452. <https://doi.org/10.1038/s41598-017-03787-6>.
- Li, H., Li, Z.P., Wan, W.J., Zhou, K., Liao, X.Y., Yang, S.J., Wang, C.J., Cao, J.C., and Zeng, H.P. (2020). Toward compact and real-time terahertz dual-comb spectroscopy employing a self-detection scheme. *ACS Photonics* 7, 49–56. <https://doi.org/10.1021/acsp Photonics.9b01427>.
- Liewald, C., Mastel, S., Hesler, J., Huber, A.J., Hillenbrand, R., and Keilmann, F. (2018). All-electronic terahertz nanoscopy. *Optica* 5, 159. <https://doi.org/10.1364/OPTICA.5.000159>.
- Madapu, K.K., Sivadasan, A.K., Baral, M., and Dhara, S. (2018). Observation of surface plasmon polaritons in 2D electron gas of surface electron accumulation in InN nanostructures. *Nanotechnology* 29, 257707. <https://doi.org/10.1088/1361-6528/aabe60>.
- Mastel, S., Lundeberg, M.B., Alonso-González, P., Gao, Y., Watanabe, K., Taniguchi, T., Hone, J., Koppens, F.H.L., Nikitin, A.Y., and Hillenbrand, R. (2017). Terahertz nanofocusing with cantilevered terahertz-resonant antenna tips. *Nano Lett.* 17, 6526–6533. <https://doi.org/10.1021/acsnanolett.7b01924>.
- Mastel, S., Goyadinov, A.A., Maissen, C., Chuvin, A., Berger, A., and Hillenbrand, R. (2018). Understanding the image contrast of material boundaries in IR nanoscopy reaching 5 nm spatial resolution. *ACS Photonics* 5, 3372–3378. <https://doi.org/10.1021/acsp Photonics.8b00636>.
- McLeod, A.S., Kelly, P., Goldflam, M.D., Gainsforth, Z., Westphal, A.J., Dominguez, G., Thieme, M.H., Fogler, M.M., and Basov, D.N. (2014). Model for quantitative tip-enhanced spectroscopy and the extraction of nanoscale-resolved optical constants. *Phys. Rev. B* 90, 085136. <https://doi.org/10.1103/PhysRevB.90.085136>.
- Moon, K., Jung, E., Lim, M., Do, Y., and Han, H. (2011). Quantitative analysis and measurements of nearfield interactions in terahertz microscopes. *Opt. Express* 19, 11539. <https://doi.org/10.1364/OE.19.011539>.
- Moon, K., Park, H., Kim, J., Do, Y., Lee, S., Lee, G., Kang, H., and Han, H. (2015). Subsurface nanoimaging by broadband terahertz pulse near-field microscopy. *Nano Lett.* 15, 549. <https://doi.org/10.1021/nl503998v>.
- Mooshammer, F., Huber, M.A., Sandner, F., Plankl, M., Zizlsperger, M., and Huber, R. (2020). Quantifying nanoscale electromagnetic fields in near-field microscopy by fourier demodulation analysis. *ACS Photonics* 7, 344–351. <https://doi.org/10.1021/acsp Photonics.9b01533>.

Nagatsuma, T.D. (2011). Terahertz technologies: present and future *IEICE Electron. Express* 8, 1127–1142. <https://doi.org/10.1587/elex.8.1127>.

Novikova, A., Markl, D., Zeitler, J.A., Rades, T., and Leopold, C.S. (2018). A non-destructive method for quality control of the pellet distribution within a MUPS tablet by terahertz pulsed imaging. *Eur. J. Pharmaceut. Sci.* 111, 549–555. <https://doi.org/10.1016/j.ejps.2017.10.029>.

Ok, G., Park, K., Lim, M.C., Kim, H.J., Chun, H.S., and Choi, S.W. (2014). High-speed terahertz imaging toward food quality inspection. *Appl. Opt.* 53, 1406. <https://doi.org/10.1364/AO.53.001406>.

Pogna, E.A.A., Silvestri, C., Columbo, L.L., Brambilla, M., Scamarcio, G., and Vitiello, M.S. (2021). Terahertz near-field nanoscopy based on detectorless laser feedback interferometry under different feedback regimes. *APL Photon* 6, 061302. <https://doi.org/10.1063/5.0048099>.

Qiu, F.C., Fu, Y.Z., Wang, C., Tan, Z.Y., Fu, Z.L., Wan, W.J., and Cao, J.C. (2019). Fast terahertz reflective confocal scanning imaging with a quantum cascade laser and a photodetector. *Appl. Phys. B-Lasers O* 125, 86. <https://doi.org/10.1007/s00340-019-7198-8>.

Schmidt, P., Vialla, F., Latini, S., Massicotte, M., Tielrooij, K.J., Mastel, S., Navickaite, G., Danovich, M., Ruiz-Tijerina, D.A., Yelgel, C., et al. (2018). Nano-imaging of intersubband transitions in van der Waals quantum wells. *Nanotechnology* 13, 1041. <https://doi.org/10.1038/s41565-018-0233-9>.

Seebacher, S., Osten, W., Veiko, V.P., and Voznessenski, N.B. (2001). Inspection of nano-sized SNOM-tips by optical far-field evaluation. *Opt. Laser. Eng.* 36, 451–473. [https://doi.org/10.1016/S0143-8166\(01\)00072-0](https://doi.org/10.1016/S0143-8166(01)00072-0).

Wagner, M., Fei, Z., McLeod, A.S., Rodin, A.S., Bao, W., Iwinski, E.G., Zhao, Z., Goldflam, M., Liu, M., Dominguez, G., et al. (2014). Ultrafast and Nanoscale Plasmonic phenomena in exfoliated

graphene revealed by infrared pump–probe nanoscopy. *Nano Lett.* 14, 894. <https://doi.org/10.1021/nl4042577>.

Wang, H.X., Fu, Z.L., Shao, D.X., Zhang, Z.Z., Wang, C., Tan, Z.Y., Guo, X.G., and Cao, J.C. (2018). Broadband bias-tunable terahertz photodetector using asymmetric GaAs/AlGaAs step multi-quantum well. *Appl. Phys. Lett.* 113, 171107. <https://doi.org/10.1063/1.5046881>.

Wehmeier, L., Nörenberg, T., de Oliveira, T.V.A.G., Klopf, J.M., Yang, S.Y., Martin, L.W., Ramesh, R., Eng, L.M., and Kehr, S.C. (2020). Phonon-induced near-field resonances in multiferroic BiFeO<sub>3</sub> thin films at infrared and THz wavelengths. *Appl. Phys. Lett.* 116, 071103. <https://doi.org/10.1063/1.5133116>.

Zhang, J.W., Chen, X.Z., Mills, S., Ciavatti, T., Yao, Z.H., Mescall, R., Hu, H., Semenenko, V., Fei, Z., Li, H., et al. (2018). Terahertz nano-imaging of graphene. *ACS Photonics* 5, 2645. <https://doi.org/10.1021/acsp Photonics.8b00190>.

## STAR★METHODS

### KEY RESOURCES TABLE

REAGENT or RESOURCE	SOURCE	IDENTIFIER
Software and algorithms		
Gwyddion	Source Forge	<a href="https://sourceforge.net/projects/gwyddion/">https://sourceforge.net/projects/gwyddion/</a>
FDTD	Lumerical Solutions corporate	<a href="https://www.westgrid.ca/support/software/lumerical_fDTD_solutions">https://www.westgrid.ca/support/software/lumerical_fDTD_solutions</a>
MATLAB code	This paper	<a href="https://doi.org/10.5281/zenodo.6629933">https://doi.org/10.5281/zenodo.6629933</a>
Other		
Electric field strength data	This paper	<a href="https://doi.org/10.5281/zenodo.6622883">https://doi.org/10.5281/zenodo.6622883</a>

### RESOURCE AVAILABILITY

#### Lead contact

Further information and requests for resources should be directed to and will be fulfilled by the lead contact, Juncheng Cao ([jccao@mail.sim.ac.cn](mailto:jccao@mail.sim.ac.cn)).

#### Material availability

The study did not generate any unique reagents.

#### Data and code availability

Electric field strength data have been deposited at Zenodo and publicly available as of the date of publication. DOI is listed in the [key resources table](#). All data reported in this paper will be shared by the [lead contact](#) upon request.

The code for analysis have been deposited at Zenodo and publicly available as of the date of publication. DOI is listed in the [key resources table](#).

Any additional information required to reanalyze the data reported in this paper is available from the [lead contact](#) upon request.

### METHOD DETAILS

#### Sample growth and device fabrication

The material system of the THz QCL and THz QWP was produced by a molecular beam epitaxy (MBE) growth technique. The active region, with 76 cascade periods, of the THz QCL was based on Al<sub>0.25</sub>Ga<sub>0.75</sub>As/GaAs design. The bottom and top electrode was grown with an n-type GaAs layer (400 nm thick) and GaAs layer (50 nm thick), respectively. The MQW region of the THz QWP was made up of 30-cycle AlGaAs/GaAs (80/18nm) structure.

#### Performance characterizations of the devices

A Fourier Transform Infrared Spectrometer (FTIR) was employed to measure the emission spectrum of the THz QCL. A pair off-axis parabolic mirrors were applied to couple the THz radiation emitted from the THz QCL to the FTIR. The output power of the THz QCL was measured by a power meter of Ophir with a thermal sensor. To calibrate the photocurrent spectra of the THz QWPs, an FTIR with a Globar source was used. The current-voltage (I-V) relation of the THz QWP was measured with the voltage-sweeping mode. The up-sweep and down-sweep curves both described the phenomena of the hysteresis loop and sharp jump of the dark current which was caused by the negative differential resistance (NDR) in the voltage-sweep mode. The noise equivalent power (NEP) parameter of the THz QWP was calculated by

$$NEP = \frac{I_n}{R}$$

where  $I_n$  is the noise spectral density measured by a low noise current preamplifier (SR570) with a sensitivity of 200 nA/V,  $R$  is the peak responsivity measured by a blackbody source (cavity blackbody IR-564/301) at the temperature of 1000 K.

### Simulation of the THz near-field signal

The simulations of the tip enhancement effect were conducted by the method of moment technique implemented in the commercial solver Altair Feko. The frequency of the incident plane wave in the model was set to be 4.2 THz. A cone with various heights and an apex radius of 40 nm was used to simulate the AFM tip. Far-field radiation was calculated at different tip-sample distances when demodulated at higher harmonics of the tip oscillation frequency. Si substrate was employed to simulate the change of S2 signal with different tip lengths from 25  $\mu\text{m}$  to 300  $\mu\text{m}$ . The tip-scan was performed over a gold-Si interface.

A finite-difference-time-domain (FDTD) method was employed to numerically simulate the edge fringe formation at the frequency of 4.2 THz. The radius and length of the tip were set to be 50 nm and 80  $\mu\text{m}$ , respectively. A plane wave was illuminated on the tip with a cone opening angle of 20°.

### Data analyses

The processing and analyses of AFM and THz imaging data were performed using Gwyddion. The fitting of THz near-field signal and processing of FDTD data were achieved using MATLAB.